INTERNATIONAL JOURNAL FOR NUMERICAL METHODS IN FLUIDS, VOL. 19, 295–319 (1994)

DEVELOPMENT OF THE DIRECT STRESS SOLUTION TECHNIQUE FOR THREE-DIMENSIONAL HYDRODYNAMIC MODELS USING FINITE ELEMENTS

RICHARD A. LUETTICH JR. AND SHENDING HU

University of North Carolina at Chapel Hill, Institute of Marine Sciences, 3431 Arendell St., Morehead City, NC 28557, U.S.A.

AND

JOANNES J. WESTERINK

Department of Civil Engineering and Geological Sciences, University of Notre Dame, Notre Dame, IN 46556, U.S.A.

SUMMARY

Velocity varies rapidly near sheared boundaries. Therefore in many practical fluid problems it can be inefficient to solve discrete equations with velocity as the dependent variable. Conversely, shear stress varies slowly near sheared boundaries, suggesting that it may be well suited for use as the dependent variable in discrete equations.

This paper describes a formulation of the internal mode equations for a three-dimensional hydrodynamic model using shear stress as the dependent variable. The resulting direct stress solution (DSS), coupled with a spatial discretization using linear finite elements, yields a system matrix that can be set up and solved with the efficiency of a banded matrix with bandwidth 8. If the eddy viscosity distribution is assumed to be piecewise linear over the depth (with an arbitrary number of time-varying segments), the recovery of velocity from stress can be easily accomplished *in closed form*, thereby avoiding any difficulty resulting from the logarithmic singularity in the velocity profile that occurs at a boundary.

Results from tidal and wind-driven test cases with realistic boundary layers are used to demonstrate the accuracy and computational advantages of a DSS formulation versus a standard velocity-based formulation.

KEY WORDS Three-dimensional circulation model Direct stress solution Internal mode solution Velocity profile - Boundary layers Tidal flow Wind-driven flow Finite element method

INTRODUCTION

Most three-dimensional surface water circulation models are based on the turbulent Reynolds equations simplified using the hydrostatic pressure approximation. The form of the resulting conservation-of-momentum equations encourages the decomposition of the three-dimensional problem into coupled problems in the horizontal and vertical directions. The solutions to the horizontal and vertical problems are commonly referred to as 'external mode' and 'internal mode' solutions respectively. The external mode solution consists of the free surface elevation and can also include the depth-averaged velocity. These solutions are usually obtained by discretizing the horizontal problem on either a finite difference grid[1–7] or a finite element grid.[8–10] The primary result obtained from the internal mode solution is the vertical profile of velocity. Internal mode solutions have been obtained by discretizing the vertical problem using

CCC 0271–2091/94/160295–25

Received 7 September 1993
Revised 12 January 1994

finite difference methods,[1-3,5,6,11] finite element methods[8-10] and spectral methods.[4,7,12-14] A common feature of virtually all three-dimensional models is that they use velocity as the dependent variable in the internal mode solution. (This approach will be called a velocity solution or VS.)

Luettich and Westerink,[15] hereafter LW, proposed an alternative internal mode solution strategy in which shear stress was used as the dependent variable in the internal mode problem. (LW termed this a direct stress solution or DSS.) The rationale behind developing the DSS technique was that velocity varies rapidly near sheared boundaries. This behaviour is difficult to represent using discrete VS equations. Conversely, shear stress varies slowly near boundaries, suggesting that its variation can be efficiently reproduced by discrete equations. Thus for coastal and shelf applications in which the surface and bottom boundary layers occupy most or all of the water column, a DSS approach may be more efficient than a VS approach for obtaining the internal mode solution.

The DSS internal mode equations presented by LW were formulated by subtracting the depth-averaged momentum equations from the three-dimensional momentum equations. A standard eddy viscosity hypothesis was used to relate shear stress and horizontal velocity:

$$\frac{\tau_z}{\rho_0} = E_z \frac{\partial \mathbf{V}}{\partial z}, \tag{1}$$

where τ_z is the vertical shear stress vector, ρ_0 is a reference density, E_z is the vertical eddy viscosity, $\mathbf{V}$ is the horizontal velocity vector and z is the vertical co-ordinate direction. Equation (1) was inverted to give

$$\frac{\partial \mathbf{V}}{\partial z} = \frac{\tau_z}{E_z \rho_0}. \tag{2}$$

Integrating equation (2) and separating the total velocity into the depth-averaged component and the deviation over the vertical yielded an expression for the velocity deviation in terms of shear stress:

$$\mathbf{V}' = \mathbf{V}_b - \bar{\mathbf{V}} + \int_{-h}^{z} \frac{\tau_z}{E_z \rho_0} \, dz, \tag{3}$$

where $\mathbf{V}'$ is the velocity deviation ($\mathbf{V}' \equiv \mathbf{V} - \bar{\mathbf{V}}$), $\bar{\mathbf{V}}$ is the depth-averaged velocity, $\mathbf{V} = \mathbf{V}_b$ at the bottom and $z = -h$ at the bottom. Equation (3) was then used to change the dependent variables in the internal mode equations from velocity deviations to shear stresses. The resulting equations were solved using a Galerkin–spectral discretization over the vertical with Legendre polynomials as expansion functions.

There are two primary disadvantages with the DSS formulation of LW. First, the equation formulation and the Galerkin–spectral discretization using polynomial expansion functions result in a fully populated system matrix. In a time-stepping model the system matrix has to be set up, decomposed and solved every time step. This requires $O(N^3)$ operations per time step, where N is the number of degrees of freedom (in this case the number of polynomials) in the discretization. By comparison, efficient VS formulations result in banded system matrices (bandwidth 6) that can be set up, decomposed and solved in $O(N)$ operations per time step.[9] Therefore, while a DSS might require fewer degrees of freedom than a VS, the VS could still require less computational effort. The second problem is due to the integrals introduced into the DSS internal mode equations by equation (3). If E_z is assumed to vary with distance from

a sheared boundary (a physically realistic variation of E_z),[16–19] the quotient τ_z/E_z has a logarithmic singularity at the boundary. Therefore a numerical evaluation of the integrals introduced by equation (3) is problematic. However, if both τ_z and E_z have polynomial variations over the depth, all integrals can be evaluated *in closed form*. LW assumed that E_z was linear over the depth, although this can easily be generalized by allowing E_z to be a continuous, piecewise linear function of depth. Unfortunately, owing to the large number of terms that occur in the closed form integration, round-off errors overwhelm the correct solution when more than five or six Legendre polynomials are used in the discretization together with more than two or three E_z segments.

We note that if the DSS equation formulation of LW is used with a Galerkin–finite element discretization, the resulting system matrix is nearly triangular and requires $O(N^2)$ operations to set up and solve per time step. The problem with round-off error contaminating the closed form solution to the integrals introduced by equation (3) is also eliminated. However, as detailed below, we have been able to develop a new DSS formulation that, when coupled with a Galerkin–finite element discretization, generates a system matrix that can be solved with $O(N)$ operations per time step and therefore is competitive with a VS on a per node basis. The present paper describes the development of this new DSS formulation and provides results from characteristic tidal and wind-driven test problems using realistic, multilayered variations in E_z.

DEVELOPMENT OF VS AND DSS INTERNAL MODE EQUATIONS

Using a general bottom- and surface-following 'σ'—co-ordinate system and assuming a hydrostatic pressure distribution and a constant density fluid, the horizontal momentum equations are

$$\frac{\partial u}{\partial t} + u\frac{\partial u}{\partial x} + v\frac{\partial u}{\partial y} + w\frac{\partial u}{\partial \sigma} - fv = -g\frac{\partial \zeta}{\partial x} + \frac{a-b}{H\rho_0}\frac{\partial \tau_{zx}}{\partial \sigma} + m_x, \tag{4a}$$

$$\frac{\partial v}{\partial t} + u\frac{\partial v}{\partial x} + v\frac{\partial v}{\partial y} + w\frac{\partial v}{\partial \sigma} + fu = -g\frac{\partial \zeta}{\partial y} + \frac{a-b}{H\rho_0}\frac{\partial \tau_{zy}}{\partial \sigma} + m_y, \tag{4b}$$

where a and b are the values of σ at the free surface and bottom respectively, f is the Coriolis parameter, g is the acceleration due to gravity, $H(x, y, t) \equiv \zeta + h$ is the total water depth, $h(x, y)$ is the bathymetric depth, m_x, $m_y(x, y, \sigma, t)$ are the horizontal momentum diffusion terms, t is the time, u, $v(x, y, \sigma, t)$ are the mean velocity components in the x- and y-directions respectively, $w(x, y, \sigma, t) \equiv d\sigma/dt$ is the vertical velocity in the 'σ'-co-ordinate system,[3,4,7] x and y are the horizontal co-ordinate directions, z is the vertical co-ordinate direction (positive upwards), $\zeta(x, y, t)$ is the free surface departure from the still water level, ρ_0 is a constant reference density of water, $\sigma \equiv b + [(a-b)/H](z+h)$ is the stretched vertical co-ordinate and τ_{zx}, $\tau_{zy}(x, y, \sigma, t)$ are the vertical shear stresses aligned in the x- and y-direction respectively. (Note that horizontal derivatives in equations (4a, b) are taken along constant 'σ' surfaces. For completeness the horizontal momentum diffusion terms have been included in equations (4a, b), although for compactness they have been represented in symbolic form. Specific expressions for these terms are readily available.[3])

Boundary conditions for equations (4a, b) are

$$\tau_{zx} = \tau_{sx} \quad \text{and} \quad \tau_{zy} = \tau_{sy} \quad \text{at } \sigma = a, \tag{5a}$$

$$\tau_{zx} = \tau_{bx} = \rho_0 k u_b \quad \text{and} \quad \tau_{zy} = \tau_{by} = \rho_0 k v_b \quad \text{at } \sigma = b, \tag{5b}$$

where k is a slip coefficient, u_b, $v_b(x, y, t) \equiv u, v(x, y, \sigma = b, t)$ are the components of the bottom slip velocity, τ_{bx}, $\tau_{by}(x, y, t) \equiv \tau_{zx}, \tau_{zy}(x, y, \sigma = b, t)$ are the components of the bottom stress and τ_{sx}, $\tau_{sy}(x, y, t) \equiv \tau_{zx}, \tau_{zy}(x, y, \sigma = a, t)$ are the components of the surface stress. A linear slip bottom boundary condition is obtained by keeping k in equation (5b) constant in time. A quadratic slip bottom boundary condition is obtained by setting $k = k'(u_b^2 + v_b^2)^{1/2}$, where k' is constant in time, A no-slip bottom boundary condition is obtained when $k = \infty$.

The general eddy viscosity formulation in equation (1) is used to relate the vertical shear stress and the horizontal velocity. In sigma co-ordinates this gives

$$\frac{\tau_{zx}}{\rho_0} = \frac{a-b}{H} E_z \frac{\partial u}{\partial \sigma} \quad \text{and} \quad \frac{\tau_{zy}}{\rho_0} = \frac{a-b}{H} E_z \frac{\partial v}{\partial \sigma}. \tag{6}$$

A typical VS internal mode formulation is obtained by substituting equation (6) into equations (4a, b) and (5a, b):

$$\frac{\partial u}{\partial t} + u\frac{\partial u}{\partial x} + v\frac{\partial u}{\partial y} + w\frac{\partial u}{\partial \sigma} - fv = -g\frac{\partial \zeta}{\partial x} + \left(\frac{a-b}{H}\right)^2 \frac{\partial}{\partial \sigma}\left(E_z \frac{\partial u}{\partial \sigma}\right) + m_x, \tag{7a}$$

$$\frac{\partial v}{\partial t} + u\frac{\partial v}{\partial x} + v\frac{\partial v}{\partial y} + w\frac{\partial v}{\partial \sigma} + fu = -g\frac{\partial \zeta}{\partial y} + \left(\frac{a-b}{H}\right)^2 \frac{\partial}{\partial \sigma}\left(E_z \frac{\partial v}{\partial \sigma}\right) + m_y, \tag{7b}$$

$$\frac{a-b}{H} E_z \frac{\partial u}{\partial \sigma}\bigg|_{\sigma=a} = \frac{\tau_{sx}}{\rho_0} \quad \text{and} \quad \frac{a-b}{H} E_z \frac{\partial v}{\partial \sigma}\bigg|_{\sigma=a} = \frac{\tau_{sy}}{\rho_0}, \tag{7c}$$

$$\frac{a-b}{H} E_z \frac{\partial u}{\partial \sigma}\bigg|_{\sigma=b} = ku_b \quad \text{and} \quad \frac{a-b}{H} E_z \frac{\partial v}{\partial \sigma}\bigg|_{\sigma=b} = kv_b. \tag{7d}$$

Equations (7a–d) can be solved for the dependent variables u and v provided that τ_{sx} and τ_{sy} are specified and $\partial\zeta/\partial x$ and $\partial\zeta/\partial y$ are known from the external mode solution.

Our new DSS internal mode formulation is obtained by first differentiating the horizontal momentum equations with respect to σ and using the chain rule (this is illustrated for the x-momentum equation (4a) only):

$$\frac{\partial}{\partial t}\left(\frac{\partial u}{\partial \sigma}\right) + u\frac{\partial}{\partial x}\left(\frac{\partial u}{\partial \sigma}\right) + \frac{\partial u}{\partial \sigma}\frac{\partial u}{\partial x} + v\frac{\partial}{\partial y}\left(\frac{\partial u}{\partial \sigma}\right) + \frac{\partial v}{\partial \sigma}\frac{\partial u}{\partial y} + \frac{\partial}{\partial \sigma}\left(w\frac{\partial u}{\partial \sigma}\right) - f\frac{\partial v}{\partial \sigma} = \frac{a-b}{H\rho_0}\frac{\partial^2 \tau_{zx}}{\partial \sigma^2} + \frac{\partial m_x}{\partial \sigma}. \tag{8}$$

Rewriting equation (6) as

$$\frac{\partial u}{\partial \sigma} = \frac{H}{a-b}\frac{\tau_{zx}}{E_z \rho_0} \quad \text{and} \quad \frac{\partial v}{\partial \sigma} = \frac{H}{a-b}\frac{\tau_{zy}}{E_z \rho_0}, \tag{9}$$

substituting these expressions into equation (8) and simplifying with the three-dimensional continuity equation gives

$$\frac{\partial}{\partial t}\left(\frac{H\tau_{zx}}{E_z(a-b)\rho_0}\right) - \frac{fH\tau_{zy}}{E_z(a-b)\rho_0} - \frac{a-b}{H\rho_0}\frac{\partial^2 \tau_{zx}}{\partial \sigma^2} = -\frac{\partial}{\partial x}\left(\frac{uH\tau_{zx}}{E_z(a-b)\rho_0}\right) - \frac{\partial}{\partial y}\left(\frac{vH\tau_{zx}}{E_z(a-b)\rho_0}\right)$$
$$- \frac{\partial}{\partial \sigma}\left(\frac{wH\tau_{zx}}{E_z(a-b)\rho_0}\right) + \frac{H\tau_{zx}}{E_z(a-b)\rho_0}\frac{\partial v}{\partial y} - \frac{H\tau_{zy}}{E_z(a-b)\rho_0}\frac{\partial u}{\partial y} + \frac{\partial m_x}{\partial \sigma}. \tag{10}$$

Using the expansions

$$\frac{\partial}{\partial\sigma}\left(\frac{wH\tau_{zx}}{E_z(a-b)\rho_0}\right)=\frac{wH}{(a-b)\rho_0}\frac{\partial}{\partial\sigma}\left(\frac{\tau_{zx}}{E_z}\right)-\frac{\tau_{zx}}{E_z(a-b)\rho_0}\left(\frac{\partial H}{\partial t}+\frac{\partial uH}{\partial x}+\frac{\partial vH}{\partial y}\right), \tag{11a}$$

$$\frac{\partial}{\partial t}\left(\frac{H\tau_{zx}}{E_z(a-b)\rho_0}\right)=\frac{H}{(a-b)\rho_0}\frac{\partial}{\partial t}\left(\frac{\tau_{zx}}{E_z}\right)+\frac{\tau_{zx}}{E_z(a-b)\rho_0}\frac{\partial H}{\partial t}, \tag{11b}$$

$$\frac{\partial}{\partial x}\left(\frac{uH\tau_{zx}}{E_z(a-b)\rho_0}\right)=\frac{uH}{(a-b)\rho_0}\frac{\partial}{\partial x}\left(\frac{\tau_{zx}}{E_z}\right)+\frac{\tau_{zx}}{E_z(a-b)\rho_0}\frac{\partial uH}{\partial x}, \tag{11c}$$

$$\frac{\partial}{\partial y}\left(\frac{vH\tau_{zx}}{E_z(a-b)\rho_0}\right)=\frac{vH}{(a-b)\rho_0}\frac{\partial}{\partial y}\left(\frac{\tau_{zx}}{E_z}\right)+\frac{\tau_{zx}}{E_z(a-b)\rho_0}\frac{\partial vH}{\partial y}, \tag{11d}$$

equation (10) can be written as

$$\frac{\partial}{\partial t}\left(\frac{\tau_{zx}}{E_z\rho_0}\right)-\frac{f\tau_{zy}}{E_z\rho_0}-\frac{(a-b)^2}{H^2\rho_0}\frac{\partial^2\tau_{zx}}{\partial\sigma^2}=A_x+\frac{a-b}{H}\frac{\partial m_x}{\partial\sigma}. \tag{12a}$$

A similar manipulation of the y-momentum equation gives

$$\frac{\partial}{\partial t}\left(\frac{\tau_{zy}}{E_z\rho_0}\right)+\frac{f\tau_{zx}}{\rho_0}-\frac{(a-b)^2}{H^2\rho_0}\frac{\partial^2\tau_{zy}}{\partial\sigma^2}=A_y+\frac{a-b}{H}\frac{\partial m_y}{\partial\sigma}. \tag{12b}$$

In equations (12a, b) A_x and A_y represent the non-linear advective terms:

$$A_x=-u\frac{\partial}{\partial x}\left(\frac{\tau_{zx}}{E_z\rho_0}\right)-v\frac{\partial}{\partial y}\left(\frac{\tau_{zx}}{E_z\rho_0}\right)-w\frac{\partial}{\partial\sigma}\left(\frac{\tau_{zx}}{E_z\rho_0}\right)+\frac{\tau_{zx}}{E_z\rho_0}\frac{\partial v}{\partial y}-\frac{\tau_{zy}}{E_z\rho_0}\frac{\partial u}{\partial y}, \tag{13a}$$

$$A_y=-u\frac{\partial}{\partial x}\left(\frac{\tau_{zy}}{E_z\rho_0}\right)-v\frac{\partial}{\partial y}\left(\frac{\tau_{zy}}{E_z\rho_0}\right)-w\frac{\partial}{\partial\sigma}\left(\frac{\tau_{zy}}{E_z\rho_0}\right)+\frac{\tau_{zy}}{E_z\rho_0}\frac{\partial u}{\partial x}-\frac{\tau_{zx}}{E_z\rho_0}\frac{\partial v}{\partial x}. \tag{13b}$$

Once τ_{zx} and τ_{zy} are determined from equations (12a, b), velocity is obtained by integrating equation (6):

$$u(\sigma)=u_b+\frac{H}{a-b}\int_b^\sigma\frac{\tau_{zx}}{E_z\rho_0}\,d\sigma \quad\text{and}\quad v(\sigma)=v_b+\frac{H}{a-b}\int_b^\sigma\frac{\tau_{zy}}{E_z\rho_0}\,d\sigma. \tag{14}$$

Three boundary conditions are required to solve equations (12a, b) and (14). Two of these are obtained from equations (5a, b):

$$\tau_{zx}=\tau_{sx} \quad\text{and}\quad \tau_{zy}=\tau_{sy} \quad\text{at } \sigma=a, \tag{15a}$$

$$u_b=\tau_{bx}/\rho_0 k \quad\text{and}\quad v_b=\tau_{by}/\rho_0 k \quad\text{at } \sigma=b. \tag{15b}$$

(It is clear from equation (15b) that a no-slip condition occurs when $k=\infty$). The third boundary condition is generated by requiring the depth-averaged velocity from the internal mode solution to match the depth-averaged velocity $(\bar{u},\bar{v})$ from the external mode solution. Averaging equation (14) over the depth and using equations (15a, b) gives

$$\frac{\tau_{bx}}{k\rho_0}+\frac{H}{(a-b)^2}\int_b^a\int_b^\sigma\frac{\tau_{zx}}{E_z\rho_0}\,d\sigma\,d\sigma=\bar{u} \quad\text{and}\quad \frac{\tau_{by}}{k\rho_0}+\frac{H}{(a-b)^2}\int_b^a\int_b^\sigma\frac{\tau_{zy}}{E_z\rho_0}\,d\sigma\,d\sigma=\bar{v}. \tag{15c}$$

As was true in the DSS formulation of LW, if E_z is assumed to vary with distance from a sheared boundary, the quotient τ_z/E_z in equations (14) and (15c) has a logarithmic singularity at the boundary. If these equations must be evaluated *numerically*, much of the anticipated benefit of a DSS approach will be lost. Therefore it is critical that a spatial discretization strategy is selected that allows these integrals to be evaluated *in closed form*. The simplest, physically realistic discretization is to assume that τ_z and E_z are continuous, piecewise linear functions over the depth. This preserves the well-established variation in E_z with distance from a boundary[16-19] and suggests a finite element solution using linear basis functions for τ_z. In this case the integrals in equations (14) and (15c) are particularly easy to evaluate *in closed form*.

LINEAR, HARMONIC FORM OF THE INTERNAL MODE EQUATIONS

Most three-dimensional circulation models discretize the external and internal mode equations in time using a time-marching method. However, in the subsequent sections of this paper we focus on the performance of the VS and DSS in tidally and wind-driven linear test cases for which analytical solutions can be found. To eliminate the possibility of time discretization errors entering into the numerical results, the VS and DSS internal mode equations are written in harmonic form by assuming that

$$\chi(x, y, t) = \chi(x, y)\, e^{i\omega t}, \tag{16}$$

where $i \equiv \sqrt{(-1)}$ and χ represents all time-varying quantities, i.e. surface elevation, velocity and shear stress. The equations are also linearized by assuming that the advective and horizontal momentum diffusion terms are negligible, $\zeta \ll h$ (therefore $H \approx h$), E_z is not a function of time and either a linear slip or no-slip bottom boundary condition can be used. We note that by using a standard time discretization technique, allowing E_z and H to vary in time and substituting equation (14) into equations (13a, b) for the advective terms, the DSS internal mode solution techniques presented herein can be extended to non-linear, aperiodic flows. It should also be possible to use the DSS approach for variable density flows as well.

Using complex notation, the linearized, harmonic VS internal mode equations can be written as

$$i(\omega + f)U^+ = -g\nabla^+\zeta + \left(\frac{a-b}{H}\right)^2 \frac{\partial}{\partial\sigma}\left(E_z \frac{\partial U^+}{\partial\sigma}\right), \tag{17a}$$

$$i(\omega - f)U^- = -g\nabla^-\zeta + \left(\frac{a-b}{H}\right)^2 \frac{\partial}{\partial\sigma}\left(E_z \frac{\partial U^-}{\partial\sigma}\right), \tag{17b}$$

$$\frac{a-b}{H} E_z \frac{\partial U^+}{\partial\sigma}\bigg|_{\sigma=a} = \frac{\tau_s^+}{\rho_0} \quad \text{and} \quad \frac{a-b}{H} E_z \frac{\partial U^-}{\partial\sigma}\bigg|_{\sigma=a} = \frac{\tau_s^-}{\rho_0}, \tag{17c}$$

$$\frac{a-b}{H} E_z \frac{\partial U^+}{\partial\sigma}\bigg|_{\sigma=b} = kU_b^+ \quad \text{and} \quad \frac{a-b}{H} E_z \frac{\partial U^-}{\partial\sigma}\bigg|_{\sigma=b} = kU_b^-. \tag{17d}$$

Similarly, the linearized, harmonic DSS internal mode equations can be written as

$$i(\omega + f)\frac{\tau_z^+}{E_z} - \left(\frac{a-b}{H}\right)^2 \frac{\partial^2\tau_z^+}{\partial\sigma^2} = 0, \tag{18a}$$

$$i(\omega - f)\frac{\tau_z^-}{E_z} - \left(\frac{a-b}{H}\right)^2 \frac{\partial^2\tau_z^-}{\partial\sigma^2} = 0, \tag{18b}$$

$$\tau_z^+ = \tau_s^+ \quad \text{and} \quad \tau_z^- = \tau_s^- \quad \text{at } \sigma = a, \tag{18c}$$

$$U_b^+ = \tau_b^+/\rho_0 k \quad \text{and} \quad U_b^- = \tau_b^-/\rho_0 k \quad \text{at } \sigma = b, \tag{18d}$$

$$\frac{\tau_b^+}{k\rho_0} + \frac{H}{(a-b)^2}\int_b^a\int_b^\sigma \frac{\tau_z^+}{E_z\rho_0}\,d\sigma\,d\sigma = \bar{U}^+ \quad \text{and} \quad \frac{\tau_b^-}{k\rho_0} + \frac{H}{(a-b)^2}\int_b^a\int_b^\sigma \frac{\tau_z^-}{E_z\rho_0}\,d\sigma\,d\sigma = \bar{U}^-, \tag{18e}$$

$$U^+(\sigma) = U_b^+ + \frac{H}{a-b}\int_b^\sigma \frac{\tau_z^+}{E_z\rho_0}\,d\sigma \quad \text{and} \quad U^-(\sigma) = U_b^- + \frac{H}{a-b}\int_b^\sigma \frac{\tau_z^-}{E_z\rho_0}\,d\sigma. \tag{18f}$$

In equations (17) and (18) $U^+ \equiv (u+iv)/2$, $U^- \equiv (u-iv)/2$, $\tau_z^+ \equiv (\tau_{zx}+i\tau_{zy})/2$, $\tau_z^- \equiv (\tau_{zx}-i\tau_{zy})/2$, $\nabla^+ \equiv \frac{1}{2}(\partial/\partial x + i\,\partial/\partial y)$, $\nabla^- \equiv \frac{1}{2}(\partial/\partial x - i\,\partial/\partial y)$, the subscripts 'b' and 's' refer to bottom and surface values respectively and overbars indicate depth-averaged quantities.

Multiplying both sides of equations (18a, b) by E_z gives an alternative set of DSS equations:

$$i(\omega + f)\tau_z^+ - \left(\frac{a-b}{H}\right)^2 E_z \frac{\partial^2 \tau_z^+}{\partial\sigma^2} = 0, \tag{19a}$$

$$i(\omega - f)\tau_z^- - \left(\frac{a-b}{H}\right)^2 E_z \frac{\partial^2 \tau_z^-}{\partial\sigma^2} = 0. \tag{19b}$$

Equations (19a, b) have the form of diffusion equations for stress and provide an intuitive understanding of the physics that is represented in the DSS form of the internal mode equations. By neglecting the advective and horizontal diffusion terms in simplifying these equations, we are assuming that stress is diffused much more rapidly over the vertical than it is transported horizontally. Although the analytical solutions to equations (18a, b) and (19a, b) are identical, the numerical solutions may not be (because E_z can be a function of σ). In the results presented below, solutions to both equation sets are considered. For clarity, equations (18a, b) are called a DSS-1 formulation and equations (19a, b) are called a DSS-2 formulation.

A significant convenience realized by writing the internal mode equations in complex form is that the form of the equations for U^+ and τ_z^+ is identical to the form of the equations for U^- and τ_z^-. If $\nabla^+\zeta = \nabla^-\zeta$, the only difference between the solutions for U^+, τ_z^+ and U^-, τ_z^- is that the former depend on $\omega + f$ while the latter depend on $\omega - f$. In the following sections numerical and analytical solutions are only presented for U^+, τ_z^+ (as functions of $\omega + f$ and $\nabla^+\zeta$), since these results are also valid for U_z^-, τ_z^- for a corresponding choice of $\omega - f$ and $\nabla^-\zeta$.

SPATIAL DISCRETIZATION OF THE INTERNAL MODE EQUATIONS

A Galerkin–finite element discretization is used over the vertical for both the VS and DSS internal mode equations.

In the VS equations velocity is expanded as

$$\hat{U}(x, y, \sigma) \equiv \sum_{n=1}^{N} \phi_n(\sigma)\hat{U}_n(x, y), \tag{20}$$

where $\hat{U}$ is the discrete approximation to U and $\hat{U}_n$ is the value of $\hat{U}$ at node n. The ϕ_n are linear chapeau functions[20] and N is the total number of nodes over the vertical. Applying the Galerkin method to equation (17a) gives

$$\int_b^a i(\omega + f)\hat{U}^+\phi_m\,d\sigma + g\nabla^+\zeta\int_b^a \phi_m\,d\sigma - \left(\frac{a-b}{H}\right)^2 \int_b^a \phi_m \frac{\partial}{\partial\sigma}\left(E_z\frac{\partial\hat{U}^+}{\partial\sigma}\right)d\sigma = 0, \tag{21}$$

where $m = 1, 2, \ldots, N$. Integrating the vertical diffusion term by parts gives

$$\int_b^a \phi_m \frac{\partial}{\partial\sigma}\left(E_z \frac{\partial \hat{U}^+}{\partial\sigma}\right) d\sigma = \phi_m E_z \frac{\partial \hat{U}^+}{\partial\sigma}\bigg|_b^a - \int_b^a \frac{\partial\phi_m}{\partial\sigma} E_z \frac{\partial \hat{U}^+}{\partial\sigma} d\sigma. \tag{22}$$

Substituting equations (20) and (22) into equation (21) and applying the surface and bottom boundary conditions, the spatially discretized VS internal mode equation can be written in final form: for $m = 1$

$$\sum_{n=1}^{N}\left[i(\omega + f)\hat{U}_n^+ \int_b^a \phi_1\phi_n\, d\sigma + \hat{U}_n^+\left(\frac{a-b}{h}\right)^2 \int_b^a E_z \frac{\partial\phi_1}{\partial\sigma}\frac{\partial\phi_n}{\partial\sigma} d\sigma\right] + \frac{a-b}{h} k\hat{U}_1^+ = -g\nabla^+\zeta \int_b^a \phi_1\, d\sigma, \tag{23a}$$

for $1 < m < N$

$$\sum_{n=1}^{N}\left[i(\omega + f)\hat{U}_n^+ \int_b^a \phi_m\phi_n\, d\sigma + \hat{U}_n^+\left(\frac{a-b}{h}\right)^2 \int_b^a E_z \frac{\partial\phi_m}{\partial\sigma}\frac{\partial\phi_n}{\partial\sigma} d\sigma\right] = -g\nabla^+\zeta \int_b^a \phi_m\, d\sigma \tag{23b}$$

and for $m = N$

$$\sum_{n=1}^{N}\left[i(\omega + f)\hat{U}_n^+ \int_b^a \phi_N\phi_n\, d\sigma + \hat{U}_n^+\left(\frac{a-b}{h}\right)^2 \int_b^a E_z \frac{\partial\phi_N}{\partial\sigma}\frac{\partial\phi_n}{\partial\sigma} d\sigma\right] - \frac{a-b}{h}\frac{\tau_s^+}{\rho_0} = -g\nabla^+\zeta \int_b^a \phi_N\, d\sigma. \tag{23c}$$

Equations (23a–c) comprise a tridiagonal system of N equations for $\hat{U}_n^+$. If this VS formulation is used to solve internal mode equations for u and v directly, the resulting system matrix is banded with bandwidth 6.

In the DSS equations stress is expanded as

$$\hat{\tau}_z(x, y, \sigma) \equiv \sum_{n=1}^{N} \phi_n(\sigma)\hat{\tau}_{zn}(x, y), \tag{24}$$

where $\hat{\tau}_z$ is the discrete approximation to τ_z and $\hat{\tau}_{zn}$ is the value of $\hat{\tau}_z$ at node n. Applying the Galerkin method to equations (18a) and (19a) and expanding $\hat{\tau}_z^+$ using equation (24) gives for DSS-1

$$\sum_{n=1}^{N}\left[i(\omega + f)\hat{\tau}_{zn}^+ \int_b^a \frac{\phi_m\phi_n}{E_z} d\sigma - \hat{\tau}_{zn}^+\left(\frac{a-b}{H}\right)^2 \int_b^a \phi_m \frac{\partial^2\phi_n}{\partial\sigma^2} d\sigma\right] = 0 \tag{25}$$

and for DSS-2

$$\sum_{n=1}^{N}\left[i(\omega + f)\hat{\tau}_{zn}^+ \int_b^a \phi_m\phi_n\, d\sigma - \hat{\tau}_{zn}^+\left(\frac{a-b}{H}\right)^2 \int_b^a E_z\phi_m \frac{\partial^2\phi_n}{\partial\sigma^2} d\sigma\right] = 0, \tag{26}$$

where $m = 1, 2, \ldots, N$. Integrating the second-order derivative terms by parts gives

$$\int_b^a \phi_m \frac{\partial^2\phi_n}{\partial\sigma^2} d\sigma = \phi_m \frac{\partial\phi_n}{\partial\sigma}\bigg|_b^a - \int_b^a \frac{\partial\phi_m}{\partial\sigma}\frac{\partial\phi_n}{\partial\sigma} d\sigma \tag{27}$$

for equation (25) and

$$\int_b^a E_z\phi_m \frac{\partial^2\phi_n}{\partial\sigma^2}\,d\sigma = E_z\phi_m \frac{\partial\phi_n}{\partial\sigma}\bigg|_b^a - \int_b^a \frac{\partial(E_z\phi_m)}{\partial\sigma}\frac{\partial\phi_n}{\partial\sigma}\,d\sigma \tag{28}$$

for equation (26). When $m = 1$ and $m = N$, the terms on the right-hand side of equations (27) and (28) are equal. This yields the physically unreasonable result that the second-order derivative terms are equal to zero. However, when $1 < m < N$, the first term on the right-hand side of equations (27) and (28) is zero. Therefore for $1 < m < N$ these equations can be substituted into equations (25) and (26) respectively to give for DSS-1, $1 < m < N$

$$\sum_{n=1}^{N}\left[i(\omega + f)\hat{\tau}_{zn}^{+}\int_b^a \frac{\phi_m\phi_n}{E_z}\,d\sigma + \hat{\tau}_{zn}^{+}\left(\frac{a-b}{H}\right)^2\int_b^a \frac{\partial\phi_m}{\partial\sigma}\frac{\partial\phi_n}{\partial\sigma}\,d\sigma\right] = 0 \tag{29}$$

and for DSS-2, $1 < m < N$

$$\sum_{n=1}^{N}\left[i(\omega + f)\hat{\tau}_{zn}^{+}\int_b^a \phi_m\phi_n\,d\sigma + \hat{\tau}_{zn}^{+}\left(\frac{a-b}{H}\right)^2\int_b^a \frac{\partial(E_z\phi_m)}{\partial\sigma}\frac{\partial\phi_n}{\partial\sigma}\,d\sigma\right] = 0. \tag{30}$$

In both the DSS-1 and DSS-2 formulations the boundary conditions provide equations for $m = 1$ and $m = N$. Equation (18c) is used as the $m = N$ equation

$$\hat{\tau}_{zN}^{+} = \tau_s \tag{31a}$$

and equations (18d, e) are combined to form the $m = 1$ equation

$$\frac{\hat{\tau}_{z1}^{+}}{k\rho_0} + \frac{H}{(a-b)^2}\sum_{n=1}^{N}\frac{\hat{\tau}_{zn}^{+}}{\rho_0}\int_b^a\int_b^\sigma \frac{\phi_n}{E_z}\,d\sigma\,d\sigma = \bar{U}^{+}. \tag{31b}$$

Equations (29)–(31a, b) form two alternative systems of N linear equations for $\hat{\tau}_{zn}^{+}$. Equations (29) and (31a) or equations (30) and (31a) generate a tridiagonal system matrix for the DSS-1 or DSS-2 formulation respectively. In addition, equation (31b) places non-zero entries in the first row of either the DSS-1 or DSS-2 system matrix. Therefore the storage and solution of the system matrix for either DSS formulation is comparable with that of a banded matrix with bandwidth 4. If either DSS formulation is used to solve internal mode equations for τ_{zx} and τ_{zy} directly, the resulting system matrix is comparable with a banded matrix with bandwidth 8.

To take advantage of this specific matrix form, we store only the banded part of the matrix and the additional row introduced by equation (31b). The matrix solution is accomplished using a standard banded matrix solver that we have modified to include operations on the additional row.

After stress is determined, velocity is obtained by solving

$$\hat{U}^{+}(\sigma) = \frac{\hat{\tau}_{z1}^{+}}{k\rho_0} + \frac{H}{a-b}\sum_{n=1}^{N}\frac{\hat{\tau}_{zn}^{+}}{\rho_0}\int_b^\sigma \frac{\phi_n}{E_z}\,d\sigma, \tag{32}$$

which is the discretized form of equation (18f). We re-emphasize the point that the integrals in equation (32) can readily be evaluated *in closed form* since E_z and φ_n are piecewise linear functions over the vertical. Also, the number of points and the specific location of the points over the vertical where the velocity is evaluated (using equation (32)) can be independent of the grid used to solve for stress.

Because both the VS and DSS formulations yield banded or nearly banded system matrices, the computational resources required to solve each scale linearly with the number of nodes in the vertical grid. However, when the same number of nodes is used in each solution, a VS should require about 25% less memory and CPU time than a DSS owing to its 25% smaller bandwidth. The integrals in equations (31b) and (32) add a small amount of additional overhead to a DSS; our experience has shown that a VS actually requires about 30% less CPU time than a DSS when the same number of nodes is used in each.

RESULTS FROM A TIDAL FLOW TEST PROBLEM

The behaviour of the internal mode formulations is first examined in a simulated tidal flow by considering a water body of infinite horizontal extent forced by a specified, periodic free surface gradient. A realistic bottom boundary layer is produced by using a no-slip condition at the bottom together with an eddy viscosity that varies linearly over the lower 20% of the water column and remains constant over the remainder of the depth:[16,17]

$$E_z = \kappa h U_{*b}\left(\frac{z_{0b}}{h} + \frac{\sigma - b}{a - b}\right) \quad \text{for } b \leqslant \sigma \leqslant b + 0{\cdot}2(a - b), \tag{33a}$$

$$E_z = \kappa h U_{*b}\left(\frac{z_{0b}}{h} + 0{\cdot}2\right) \quad \text{for } b + 0{\cdot}2(a - b) \leqslant \sigma \leqslant a, \tag{33b}$$

where $\kappa = 0.4$ is the von Kármán constant, z_{0b} is the effective bottom roughness and U_{*b} is the bottom friction velocity defined as

$$U_{*b} \equiv \sqrt{(|\tau_b|/\rho_0)}. \tag{34}$$

Analytical solutions for this general class of problems (although with different eddy viscosity distributions) have been presented in the literature.[18–23] The analytical solution for a water column forced by either a specified free surface gradient or a specified surface stress assuming an eddy viscosity that consists of up to three continuous linear segments over the vertical is summarized in the Appendix. Since E_z is dependent on U_{*b} (and therefore τ_b), it cannot be specified *a priori*. Rather, iteration is used until the friction velocity obtained by substituting the analytical solution for τ_b into equation (34) matches the value used in equations (33a, b).

Prior to examining the numerical solutions, it is useful to consider the characteristics of the analytical solution to this test problem. Figure 1 presents the non-dimensional ratio of the bottom stress to the surface gradient forcing as a function of the dimensionless forcing frequency $\Omega_b^+ \equiv h(\omega + f)/U_{*b}$, and the dimensionless bottom roughness z_{0b}/h. At low frequency a close balance exists between the bottom stress and the surface gradient forcing (boundary layer flow). Conversely, at high frequency the bottom stress becomes unimportant in the overall force balance and the driving force is balanced by the inertial force (quasi-geostropic flow). At intermediate frequency both the bottom stress and the inertial force are effective in balancing the surface gradient. The importance of bottom stress increases weakly with z_{0b}/h.

At low frequency or when U^+ is small, the governing internal mode equation (equation (17a)) reduces to

$$\frac{a - b}{H}\frac{\partial}{\partial \sigma}\left(\frac{\tau_z^+}{\rho_0}\right) \approx g\nabla^+\zeta. \tag{35}$$

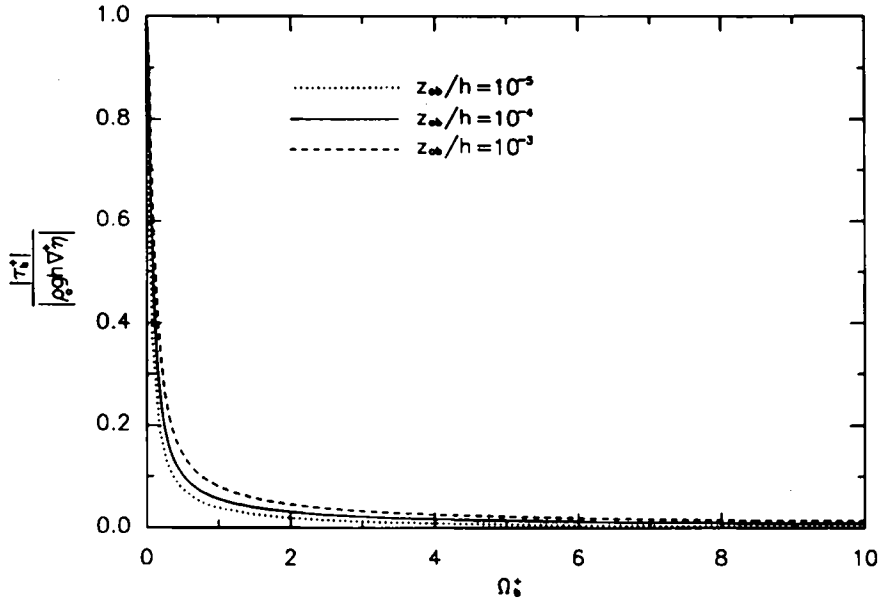

Figure 1. Dimensionless bottom stress as a function of dimensionless frequency and bottom roughness from the analytical solution to the tidal test problem

In these cases τ_z^+ is approximately linear with depth because $g\nabla^+\zeta$ is not a function of depth. Figure 2 shows the vertical distribution of non-dimensional velocity and stress (amplitude and phase) from the analytical solution for the three dimensionless frequencies $\Omega_b^+ = 0{\cdot}1$, 1 and 10 using $z_{0b}/h = 10^{-4}$. These frequencies span the range from boundary layer flow to quasi-geostropic flow. At low frequency ($\Omega_b^+ \leqslant 0{\cdot}1$) the frictional effects of the bottom boundary layer penetrate the entire water column. The velocity profile is sharply curved near the bottom and some curvature persists up to the free surface. The stress profile is nearly linear over the total depth. At high frequency ($\Omega_b^+ \geqslant 10$) the thickness of the bottom boundary layer is only a fraction of the total depth. The velocity profile is again sharply curved near the bottom, although above the bottom boundary layer the flow is quasi-geostropic as evidenced by zero stress and a constant vertical profile of velocity. The stress profile is linear only near the bottom where $U^+ \to 0$. Near the top of the boundary layer the transition from frictional to irrotational flow introduces curvature into the stress profile and a characteristic 'bulge' into the velocity amplitude profile. The transition from low to high frequency ($\Omega_b^+ \approx 1$) is characterized by the gradual development of curvature in the stress profile as the boundary layer is restricted to a fraction of the total depth.

The stress profiles shown in Figure 2 suggest that for $\Omega_b^+ \approx 1$ or less a highly accurate numerical solution should be possible using a DSS with relatively few evenly spaced nodes over the depth. For $\Omega_b^+ \approx 10$ or greater accurate DSS results should require either a larger number of evenly spaced nodes or a non-uniform node arrangement over the depth. The velocity profiles shown in Figure 2 indicate that for all Ω_b^+ a VS formulation will require considerable resolution in approximately the lower 10% of the water column. We note that a typical semidiurnal tidal flow on the continental shelf ($\omega \approx 1{\cdot}4 \times 10^{-4}\,s^{-1}$, $f \approx 1 \times 10^{-4}\,s^{-1}$, $h \approx 50$ m, $U_{*b} \approx 1$ cm s^{-1}) falls in the range of $\Omega_b^+ \approx 1$ where a DSS would be attractive.

Comparisons are presented between the analytical solution and the VS, DSS-1 and DSS-2 numerical solutions. The VS numerical solutions were forced by a specified free surface gradient

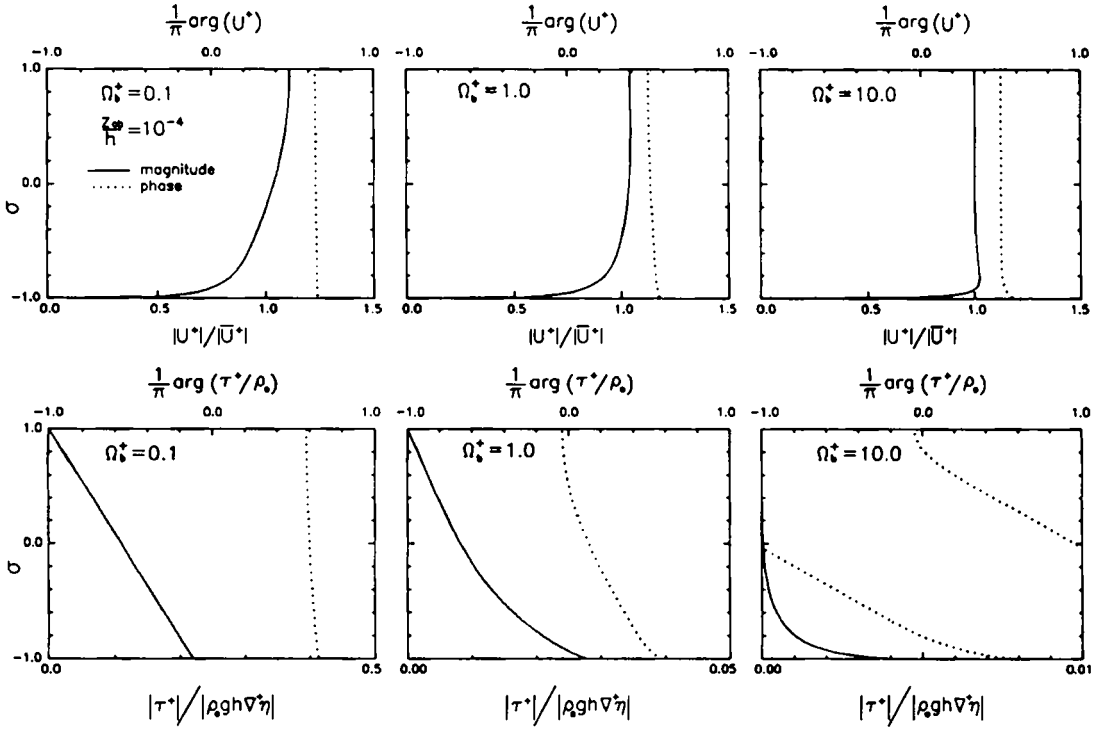

Figure 2. Vertical profiles of velocity and shear stress from the analytical solution to the tidal test problem

while the DSS numerical solutions were forced by the depth-averaged velocity that was obtained from the analytical solution for the specified free surface gradient. In each case U_{*b} from the analytical solution was used to specify the eddy viscosity. To provide as critical a test as possible, the DSS results were computed using a uniform grid over the vertical while the VS results were computed using a non-uniform grid over the vertical. For a no-slip bottom boundary condition the analytical solution for velocity approaches a logarithmic distribution as $\sigma \to b$:

$$U^+ \approx \frac{U_{*b}}{\kappa} \ln\left[\frac{h}{z_{0b}}\left(\frac{\sigma - b}{a - b}\right) + 1\right]. \tag{36}$$

Defining a new vertical co-ordinate S as

$$S \equiv \ln\left[\frac{h}{z_{0b}}\left(\frac{\sigma - b}{a - b}\right) + 1\right] \Big/ \ln\left(\frac{h}{z_{0b}} + 1\right) \tag{37}$$

allows U^+ to be written as a linear function of S near the bottom. Davies[24] converted VS momentum equations into an S-co-ordinate system similar to the one defined by equation (37) and solved the resulting equations using a uniform 'S-grid' over the vertical. For the present study equation (37) was rewritten to provide an expression for the σ-spacing that corresponds to a uniform S-spacing:

$$\sigma_n = b + (a - b)\frac{z_{0b}}{h}\left[\left(\frac{h + z_{0b}}{z_{0b}}\right)^{(n-1)\Delta S} - 1\right]. \tag{38}$$

In equation (38) $n = 1, 2, \ldots, N$ is the node number and $\Delta S \equiv 1/(N-1)$. Equation (38) was used to generate a non-uniform grid for the VS computations. We note that the non-uniform σ-grid generated by equation (38) is optimized for this test problem and would be somewhat impractical for use in an actual three-dimensional model because a different σ-spacing would be required at each horizontal location where z_{0b}/h varied.

Our initial assessment of the DSS and VS performances is based on the error in the computed bottom stress. Figures 3 and 4 present the normalized amplitude error and the phase error for the DSS-1, DSS-2 and VS numerical solutions as functions of the number of nodes used over the vertical for $z_{0b}/h = 10^{-4}$ and 10^{-3}. As expected, when a uniform grid is used, the efficiency of the DSS methods is best for moderate to low frequency (i.e. $\Omega_b^+ \leqslant 1$) and becomes rather poor at high frequency (i.e. $\Omega_b^+ \geqslant 10$). Figures 3(a)–3(d) and 4(a)–4(d) indicate that bottom roughness has little effect on the DSS results. Conversely, the VS results are nearly independent of frequency because the shape of the velocity profile in the sharply curved part near the bottom is not a function of frequency (e.g. equation (36)). The shape of the velocity profile is dependent on the roughness, however, and the VS becomes less accurate as the dimensionless roughness decreases. (Compare Figures 3(e) and 3(f) with Figures 4(e) and 4(f)). The VS bottom stress

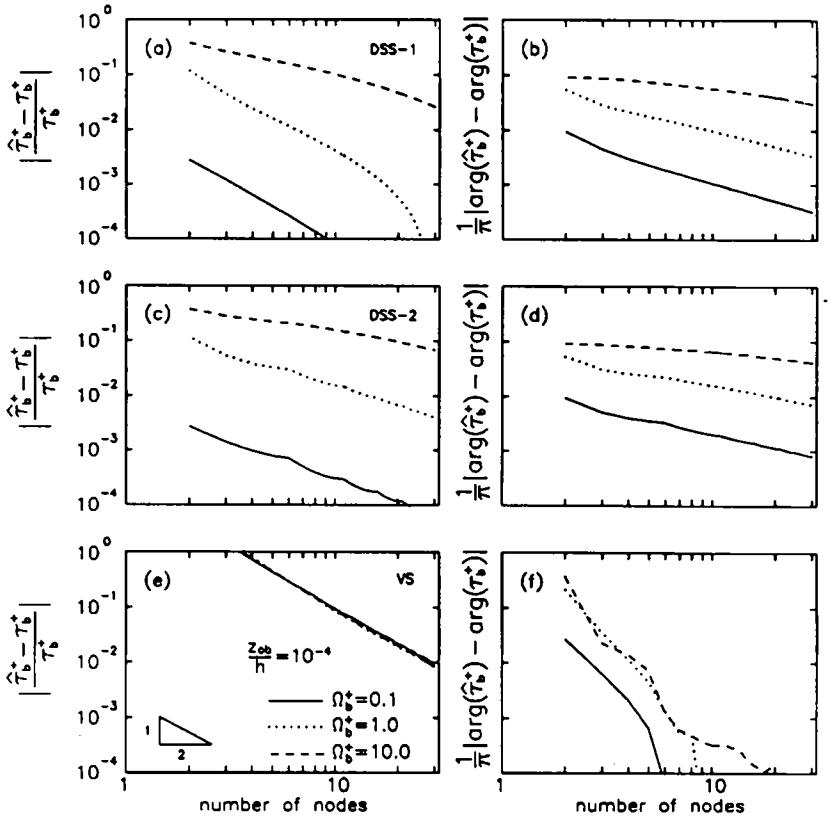

Figure 3. Convergence of bottom stress for the DSS-1, DSS-2 and VS numerical solutions to the tidal test problem for dimensionless bottom roughness $z_{0b}/h = 10^{-4}$

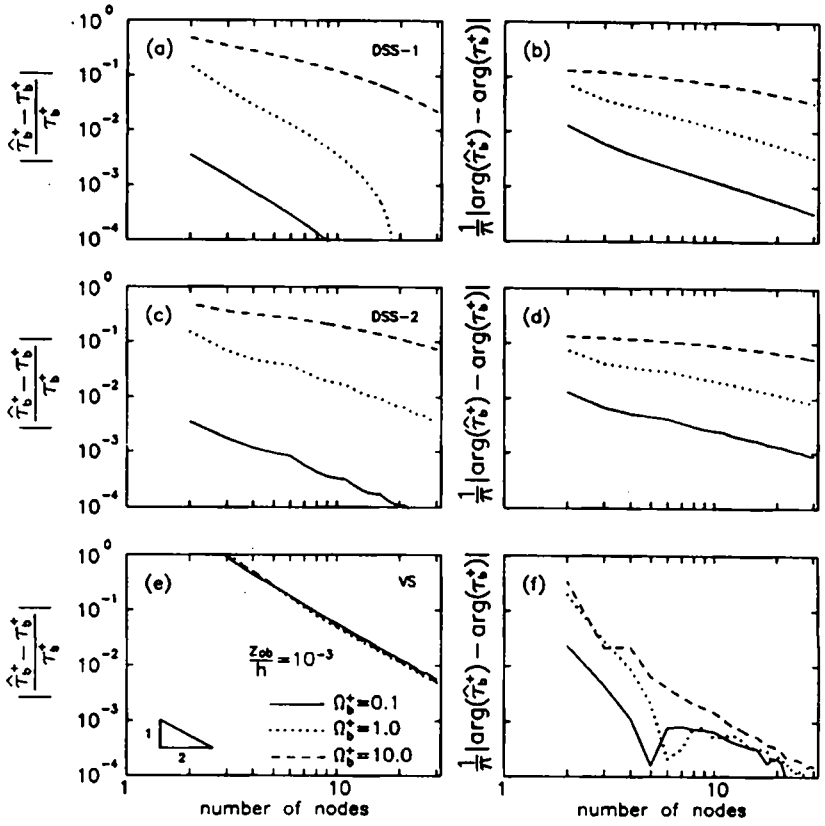

Figure 4. Convergence of bottom stress for the DSS-1, DSS-2 and VS numerical solutions to the tidal test problem for dimensionless bottom roughness $z_{ob}/h = 10^{-3}$

amplitude has a second-order convergence while the phase convergence is somewhat faster. (A second-order convergence of bottom stress amplitude was also found for a VS on a uniform grid of linear finite elements when the eddy viscosity was kept constant over the vertical.[8]) The DSS-1 method has approximately second-order convergence for amplitude for $\Omega_b^+ \leqslant 1$. The convergence rate decreases at higher frequencies and is generally poorer for phase than for amplitude. Both the rate of convergence and the absolute convergence for a given number of nodes are worse for the DSS-2 formulation than for the DSS-1 formulation.

Table I quantifies these results further by presenting the number of nodes required by each numerical solution to reach an amplitude error of 1% in bottom stress. For all frequencies and roughnesses the DSS-1 results were consistently as good as or better than the DSS-2 results. Since there is minimal difference in the CPU time or memory requirement between the two DSS formulations, the DSS-2 approach has been dropped from further consideration. For moderate to low frequencies the DSS-1 numerical solution requires considerably fewer uniformly spaced grid points to achieve the same level of accuracy as the VS numerical solution using the optimized non-uniform σ-grid.

Since the vertical profile of velocity is often the primary quantity desired from the internal mode solution, the vertical profiles of velocity from the DSS-1 and VS numerical solutions have

Table I. Bottom stress convergence summary for the tidal test problem

		Number of nodes for error < 1%		
Ω_b^+	z_{ob}/h	DSS-1	DSS-2	VS
0·1	10^{-3}	2	2	22
1·0	10^{-3}	7	15	23
10·0	10^{-3}	42	>60	23
0·1	10^{-4}	2	2	31
1·0	10^{-4}	7	15	29
10·0	10^{-4}	51	>60	29
0·1	10^{-5}	2	2	37
1·0	10^{-5}	7	13	37
10·0	10^{-5}	52	>60	37

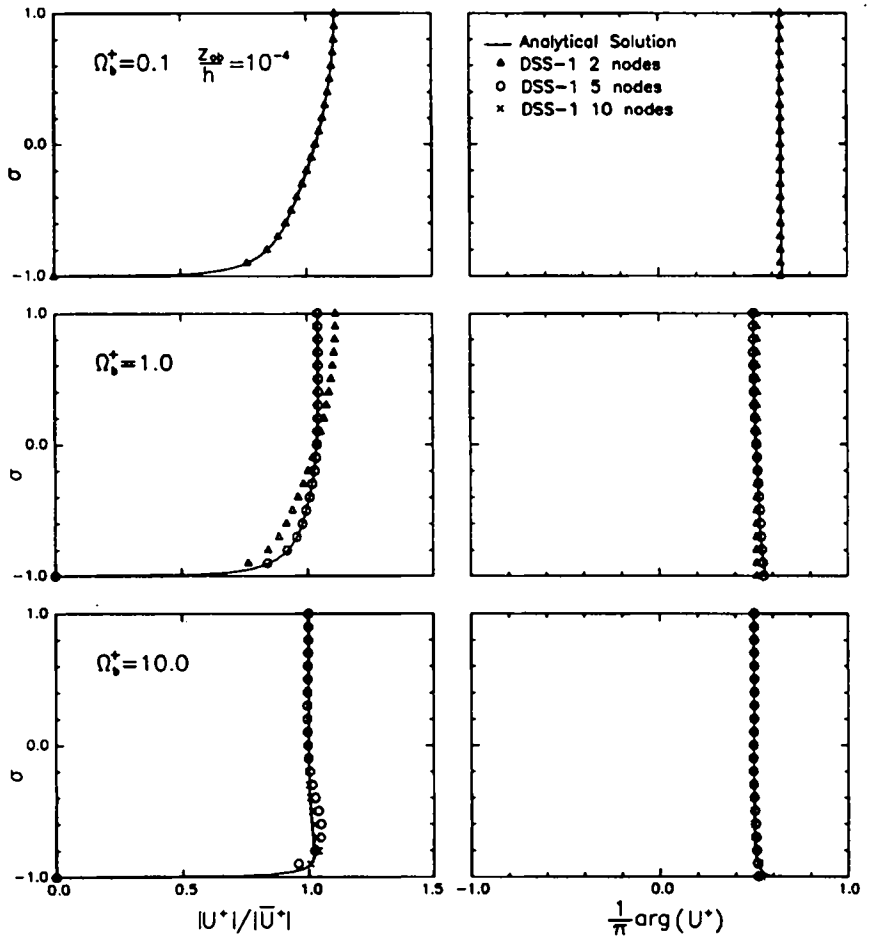

Figure 5. Convergence of the vertical profiles of velocity obtained from the DSS-1 numerical solution to the tidal test problem. For display purposes the velocity profile was evaluated at 21 evenly spaced locations over the vertical

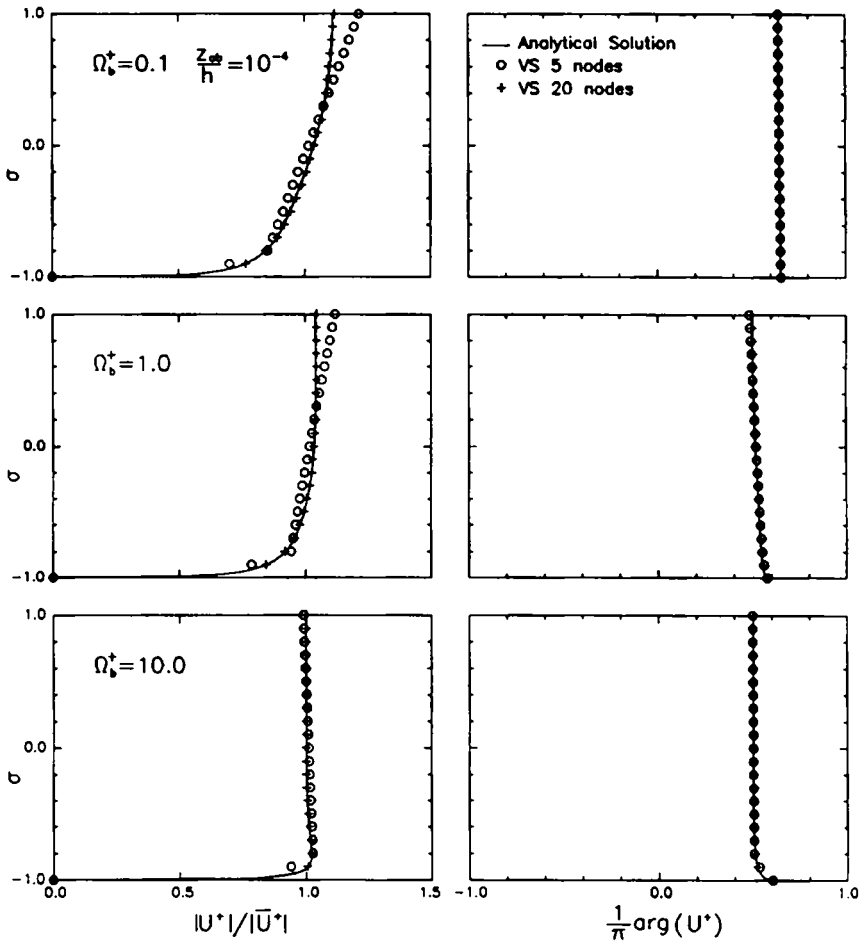

Figure 6. Convergence of the vertical profiles of velocity obtained from the VS numerical solution to the tidal test problem. For display purposes the velocity profile was interpolated at 21 evenly spaced locations over the vertical

been plotted in Figures 5 and 6 respectively. These figures illustrate the high accuracy of the DSS numerical solution for low to moderate frequencies and generally confirm the comparative performance of the DSS and VS numerical solutions indicated by the bottom stress analyses.

RESULTS FROM A WIND-DRIVEN TEST PROBLEM

The behaviour of the internal mode formulations is examined further in a simulated wind-driven flow by considering a water body of infinite horizontal extent forced by a specified, periodic free surface stress. While a periodic surface stress rarely exists in practical flows, this test problem still provides useful insight to the characteristic behaviour of the internal mode solution in wind-driven flows. Realistic surface and bottom boundary layers are produced by using a no-slip condition at the bottom together with an eddy viscosity distribution that increases linearly with distance from the free surface and bottom boundaries.[18,19] In analogy with the tidal problem,

it is assumed that the linear eddy viscosity segments that terminate at the free surface and at the bottom each occupy 20% of the depth, i.e.

$$E_z = \kappa h U_{*b}\left(\frac{z_{0b}}{h} + \frac{\sigma - b}{a - b}\right) \quad \text{for } b \leqslant \sigma \leqslant b + 0{\cdot}2(a - b), \tag{39a}$$

$$E_z = \kappa h U_{*s}\left(\frac{z_{0s}}{h} + \frac{a - \sigma}{a - b}\right) \quad \text{for } a - 0{\cdot}2(a - b) \leqslant \sigma \leqslant a, \tag{39a}$$

where z_{0s} is the effective roughness of the free surface and U_{*s} is the surface friction velocity defined as

$$U_{*s} \equiv \sqrt{(|\tau_s|/\rho_0)}. \tag{40}$$

The eddy viscosity in the remaining 60% of the water column is assumed to vary linearly and to connect the segments described in equations (39a, b). The result is a continuous, piecewise linear distribution (containing three linear segments) of eddy viscosity over the depth.

The analytical solution summarized in the Appendix also applies to the wind-driven problem. In this case U_{*s} is known (from the specified surface stress forcing); however, it is again necessary to iterate until the analytical solution for τ_b gives a value of U_{*b} that matches the value used in the eddy viscosity distribution.

The non-dimensional ratio of the bottom stress to the applied free surface stress as a function of the dimensionless forcing frequency ($\Omega_s^+ \equiv h(\omega + f)/U_{*s}$) and the dimensionless roughnesses (z_{0b}/h, z_{0s}/h) obtained from the analytical solution is presented in Figure 7. At low frequency a close balance exists between the bottom stress and the surface stress. Similar to the tidal test case, at high frequency the bottom stress becomes unimportant in the overall force balance and the driving force is balanced by the inertial force. At intermediate frequency both the bottom stress and the inertial force balance the surface stress. The importance of bottom stress increases with z_{0b}/h but is quite insensitive to z_{0s}/h. We note that we were only able to get the analytical solution to converge for a limited range of Ω_s^+ (i.e. as shown in Figure 7). We believe that this was due to round-off error in the Kelvin function routines (IMSL) used in the analytical solution.

The vertical distribution of non-dimensional velocity and stress (amplitude and phase) obtained from the analytical solution for the three dimensionless frequencies $\Omega_s^+ = 0{\cdot}01, 0{\cdot}1$ and $0{\cdot}4$ using $z_{0b}/h = 10^{-3}$ and $z_{0s}/h = 10^{-3}$ is presented in Figure 8. These frequencies span the range of force balances described above. In each case the velocity profiles are sharply curved near the bottom and free surface boundaries. At low frequency or when U^+ is small, the governing internal mode equation (equation (17a)) reduces to

$$\frac{\partial}{\partial \sigma}\left(\frac{\tau_z^+}{\rho_0}\right) \approx 0. \tag{41}$$

Equation (41) indicates that for these cases τ_z^+ is approximately independent of depth. Figure 8 shows that at low frequency the stress is essentially constant through the water column. At higher frequencies the bottom stress decreases, the stress is constant only near the bottom where $U^+ \to 0$ and the stress profile curves as it varies from a non-zero surface value to a constant value in the lower part of the water column.

The vertical stress profiles shown in Figure 8 suggest an efficient numerical solution should be possible using a DSS with evenly spaced nodes, at least for $\Omega_s^+ \leqslant 0{\cdot}4$. At substantially higher frequencies the increased curvature in the stress profile means that a DSS will require either a

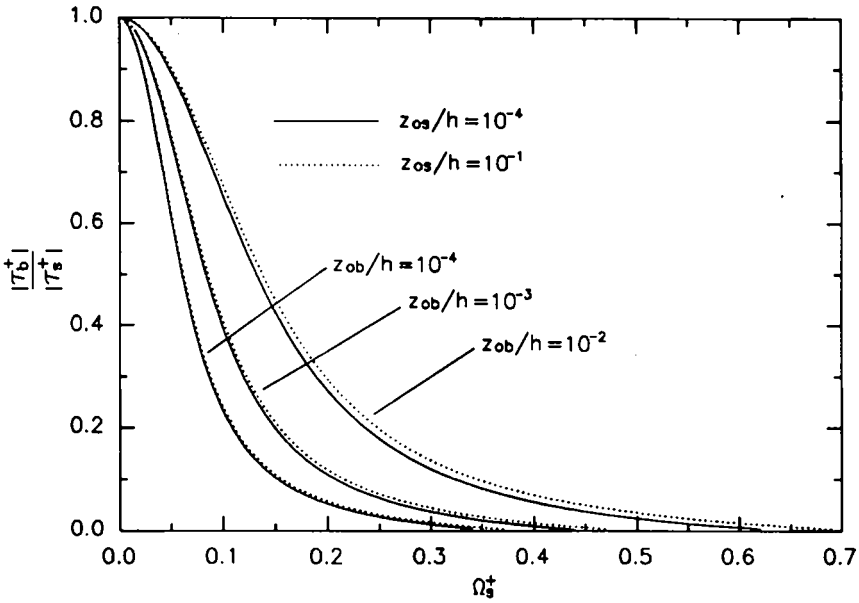

Figure 7. Dimensionless bottom stress as a function of dimensionless frequency, bottom roughness and surface roughness from the analytical solution to the wind-driven test problem

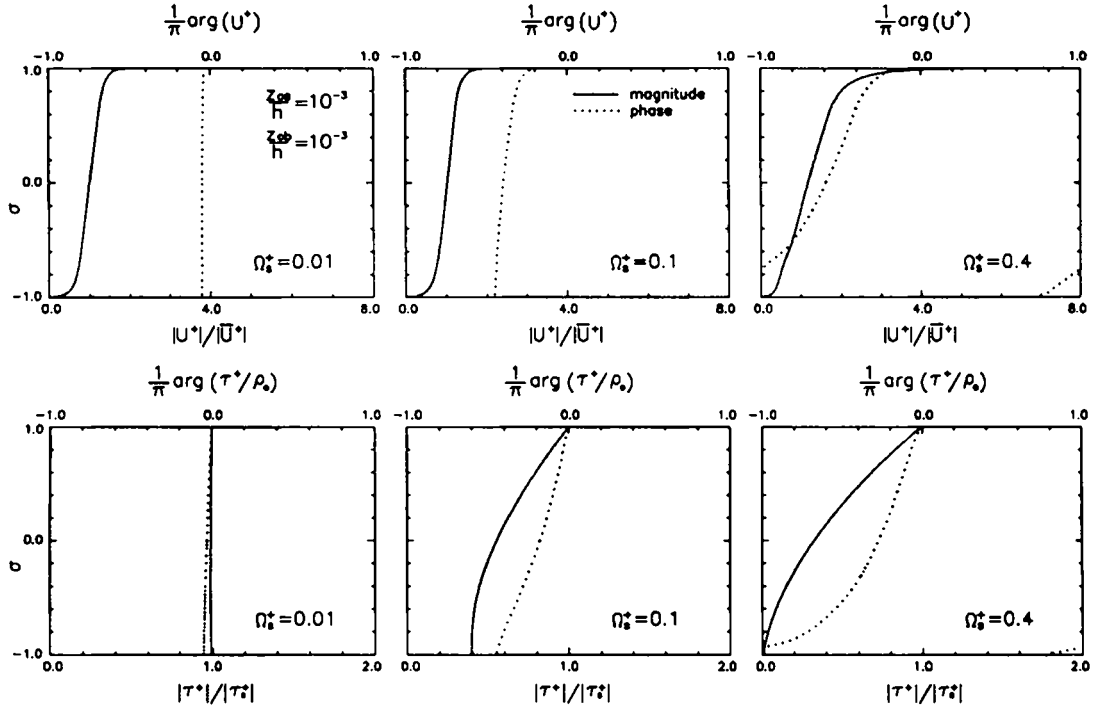

Figure 8. Vertical profiles of velocity and shear stress from the analytical solution to the wind-driven test problem

large number of evenly spaced nodes or a non-uniform node arrangement over the depth, as was true in the tidal test case. In fact, at high frequency the effects of the surface stress do not reach the bottom and only a surface boundary layer forms. At this point the wind-driven problem behaves much like the tidal test problem turned upside down. The velocity profiles in Figure 8 suggest that for all Ω_s^+ a VS formulation will require considerable resolution near both the surface and bottom boundaries. For reference, a 10 m s^{-1} wind ($U_{*s} \approx 1$ cm s^{-1}) with a 12 h period at mid-latitude ($f \approx 1 \times 10^{-4}$) in 20 m water depth would have $\Omega_s^+ \approx 0{\cdot}5$.

In the comparisons made between the VS and DSS-1 numerical solutions, the VS was forced by the specified free surface stress while the DSS-1 was forced by the specified free surface stress and the depth-averaged velocity that was obtained from the analytical solution. U_{*b} from the analytical solution along with the specified U_{*s} was used to evaluate the eddy viscosity. The DSS-1 was computed using a uniform σ-grid over the vertical. The VS was computed using a non-uniform σ-grid that was compressed near both the free surface and the bottom using an analogous form of equation (38). As noted for the tidal test case, this optimal σ-spacing would not be practical for use in an actual three-dimensional model owing to spatial and/or temporal variations in z_{0b}/h and z_{0s}/h.

Figure 9 presents the non-dimensional bottom stress as a function of the number of nodes used in the solution for the VS and the DSS-1. Similarly to the tidal test case, at low frequency (i.e. $\Omega_s^+ \leqslant 0{\cdot}1$) a highly accurate solution is obtained from the DSS-1 with two to four nodes over the depth. In this frequency range the VS requires roughly 10 times as many nodes to give the same accuracy. For $\Omega_s^+ = 0{\cdot}4$ the VS requires about twice as many nodes as with the DSS-1 for comparable accuracy. As was true in the tidal problem, we expect that at high frequency a VS on a non-uniform grid will give better results than a DSS on a uniform grid for the same number of nodes. While the bottom stress comparison is presented only for the case $z_{0b}/h = 10^{-3}$ and $z_{0s}/h = 10^{-3}$, a VS for wind-driven flows becomes less accurate as the roughness decreases (as was true for the tidal problem). Both the DSS and the VS have a second-order convergence rate (Figure 9). (Note that because the absolute value of the phase error is plotted in Figure 9,

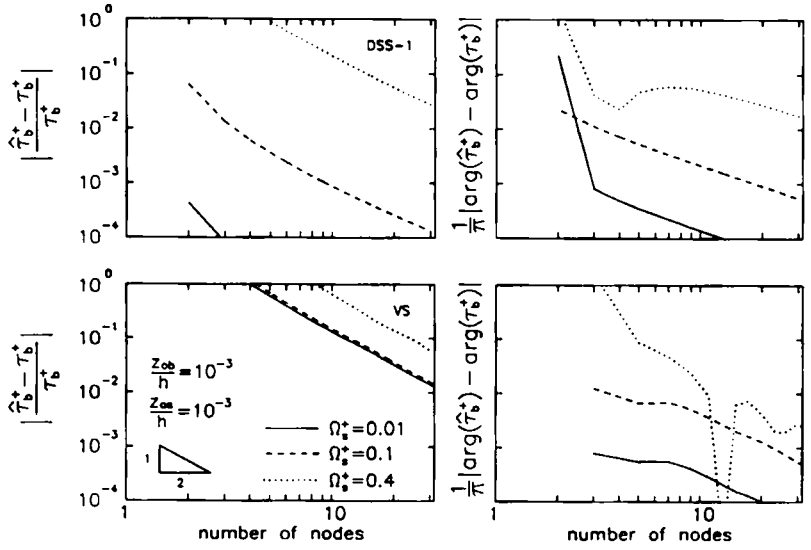

Figure 9. Convergence of bottom stress amplitude and phase for the DSS-1 and VS numerical solutions to the wind-driven test problem for dimensionless roughnesses $z_{0b}/h = 10^{-3}$ and $z_{0s}/h = 10^{-3}$

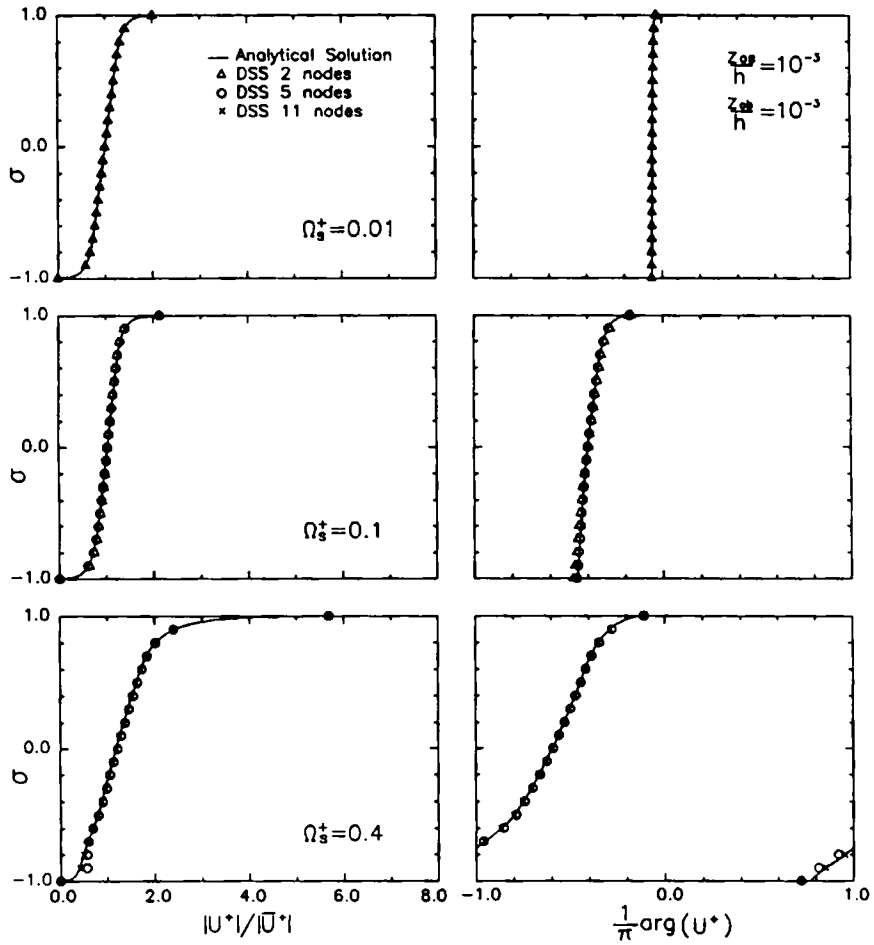

Figure 10. Convergence of the vertical profiles of velocity obtained from the DSS-1 numerical solution to the wind-driven test problem. For display purposes the velocity profile was evaluated at 21 evenly spaced locations over the vertical

a large dip occurs in the VS plot for $\Omega_s^+ = 0{\cdot}4$ when the phase error changes from positive to negative.)

Vertical profiles of velocity obtained from the DSS are shown in Figure 10. Nearly exact results are obtained with two, five and 11 nodes over the vertical for $\Omega_s^+ = 0{\cdot}01$, $0{\cdot}1$ and $0{\cdot}4$ respectively. Because the surface stress is specified as a boundary condition and the vertical stress profile is nearly linear near the free surface, the velocity profile near the surface is quite accurate for all frequencies when only two to four nodes are used over the vertical. This suggests that the DSS technique may be particularly useful for modelling near-surface currents in wind-driven flows, even at high frequency.

CONCLUSIONS

Since velocity varies rapidly near a sheared boundary, in many practical fluid problems it can be inefficient to solve discrete equations with velocity as the dependent variable. Conversely,

shear stress varies slowly near a sheared boundary, suggesting that it may well be suited for use as the dependent variable in discrete equations.

Luettich and Westerink[15] (LW) proposed a direct stress solution (DSS) technique that allowed shear stress to be used as the dependent variable in the internal mode solution of a three-dimensional hydrodynamic model. In the present paper we describe a major improvement to the earlier DSS technique. The new formulation, coupled with a spatial discretization using linear finite elements, replaces the fully populated system matrix of LW (approximately N^3 operations per time step) with a system matrix that requires comparable computational resources to store and solve as a banded matrix with bandwidth 8 (approximately N operations per time step). The most efficient velocity-based solutions (VS) generate banded system matrices with bandwidth 6. For the same number of nodes over the vertical a VS requires only about 30% less CPU time than a DSS (including extracting the velocity profile from the stress profile). If the eddy viscosity distribution is assumed to be piecewise linear over the depth (with an arbitrary number of time-varying segments), the conversion from stress to velocity, equation (32), can be done easily *in closed form*, thereby avoiding any difficulty resulting from the logarithmic singularity in the velocity profile that occurs at the boundary. The new DSS formulation also eliminates the problem with round-off error that was encountered when the LW formulation was used with more than five or six Legendre polynomials and more than two or three eddy viscosity segments.

The complete DSS formulation is presented for barotropic internal mode equations that have been simplified by neglecting non-linear terms and by assuming a harmonic solution in time. However, straightforward extensions can be made to obtain a transient, fully non-linear, three-dimensional numerical model using the DSS approach. It should also be possible to use a DSS formulation in stratified flows if this seems desirable.

Tidal and wind-driven test problems with realistic boundary layers were used to compare two variations of the new DSS formulation with a standard VS formulation. In both problems the DSS numerical solutions were obtained using a uniform grid over the vertical while the VS numerical solutions were obtained using a non-uniform grid (compressed near the bottom in the tidal problem and compressed near the surface and the bottom in the wind-driven problem). The non-uniform grids were optimized for logarithmic velocity profiles near the boundaries with specified z_{0b}/h and z_{0s}/h.

For the tidal test problem the DSS-1 formulation was found to give more accurate results than the DSS-2 formulation for all cases considered. The efficiency of a DSS is dependent on the dimensionless forcing frequency $\Omega_b \equiv (\omega \pm f)h/U_{*b}$. For $\Omega_b \leqslant 1$ (approximately) the bottom boundary layer penetrates the entire water column, the stress profile is relatively linear and the VS requires three to five times more nodes for the same accuracy as the DSS-1. For $\Omega_b \geqslant 10$ the bottom boundary layer is limited to only a fraction of the water column, significant curvature exists in the stress profile and the VS on a non-uniform grid is more efficient than a DSS on a uniform grid. We note that a DSS is particularly accurate and efficient at frequencies where the bottom stress is important in the depth-integrated force balance. The accuracy of the VS is independent of Ω_b in the range tested, although it is dependent on z_{0b}/h. The convergence rates for bottom stress for both the VS and DSS formulations are of second order.

For the wind-driven test problem the efficiency of a DSS is dependent on the dimensionless forcing frequency $\Omega_s \equiv (\omega \pm f)h/U_{*s}$. For $\Omega_s \leqslant 1$ (approximately) the surface boundary layer penetrates the entire water column, the stress profile is relatively linear and the VS again requires considerably more nodes for the same accuracy as a DSS. We were unable to obtain an analytical solution at higher values of Ω_s and therefore could not directly test the numerical technique in this range. However, for higher Ω_s the surface boundary layer becomes isolated in the upper

fraction of the water column, no bottom boundary layer develops and the wind-driven problem behaves much like an upside-down tidal problem, except that the stress at the free surface boundary is specified. Since the stress profile remains linear near this boundary, a DSS numerical solution remains accurate and efficient in the surface region. The convergence rates for bottom stress for both the VS and DSS-1 formulations are again of second order.

From a practical three-dimensional modelling perspective the use of a uniform σ-grid over the vertical will be preferable to the use of a non-uniform σ-grid over the vertical *if the latter must be optimized so that the σ-interval is a function of local variables such as h, z_{0b} and z_{0s}* (e.g. equation (38)). Since all the VS results presented above were computed on optimized, non-uniform σ-grids, the relative performances of the DSS and VS approaches that have been presented are valid only for these grids. However, the performance of a VS will clearly be diminished if a non-optimized σ-grid is used over the vertical, (i.e. a grid that has the same σ-spacing at all horizontal locations regardless of local variables).

Finally, it should be noted that in contrast with the test cases presented above, many three-dimensional hydrodynamic models do not explicitly resolve the boundary layers. Rather, they parametrize the bottom boundary layer using a slip condition and thereby avoid resolving this high-velocity-gradient region. Often the free surface boundary layer simply remains unresolved. Using these simplifications, a VS can usually be obtained on a uniform grid using as few or fewer nodes over the vertical than a DSS.[15] Therefore the main advantage of a DSS model occurs in flows dominated by the boundary layer(s) (i.e. small Ω_b and/or Ω_s) or when resolving the flow near the boundary is of particular interest.

ACKNOWLEDGEMENTS

This work was supported by the National Science Foundation Grant OCE-9116448 and by the U.S. Army Corps of Engineers Waterways Experiment Station Dredging Research Program, contract DACW39-90-K-0021.

APPENDIX: SUMMARY OF ANALYTICAL SOLUTION

In this appendix we briefly summarize the analytical solution to the linear, harmonic form of the internal mode equations for an eddy viscosity that consists of up to three continuous segments through the water column. Specifically, we solve the $\omega + f$ part of the complex internal mode equations (17a, b),

$$i(\omega + f)U^+ = -g\nabla^+\zeta + \left(\frac{a-b}{H}\right)^2 \frac{\partial}{\partial\sigma}\left(E_z \frac{\partial U^+}{\partial\sigma}\right), \tag{42}$$

with boundary conditions

$$\frac{a-b}{H} E_z \frac{\partial U^+}{\partial\sigma} = \frac{\tau_s^+}{\rho_0} \quad \text{at } \sigma = a, \tag{43a}$$

$$\frac{a-b}{H} E_z \frac{\partial U^+}{\partial\sigma} = kU_b^+ \quad \text{at } \sigma = b \tag{43b}$$

and eddy viscosity distribution

$$E_z = E_{z0}\,\phi(\sigma), \tag{44a}$$

where

$$\phi(\sigma) = \begin{cases} \phi(b) + l_1(\sigma - b), & b \leqslant \sigma \leqslant \sigma_1, \\ \phi(\sigma_1) + l_2(\sigma - \sigma_1), & \sigma_1 \leqslant \sigma \leqslant \sigma_2, \\ \phi(\sigma_2) + l_3(\sigma - \sigma_2), & \sigma_2 \leqslant \sigma \leqslant a. \end{cases} \tag{44b}$$

In equations (44a, b) $1/l_j$ is a slope constant for layer j and σ_j is the upper limit of layer j.

The solution to equations (42)–(44) can be written as

$$U^+(\sigma) = U_0^+ + \begin{cases} c_1 B_1(\sigma) + c_2 K_1(\sigma), & b \leqslant \sigma \leqslant \sigma_1, \\ c_3 B_2(\sigma) + c_4 K_2(\sigma), & \sigma_1 \leqslant \sigma \leqslant \sigma_2, \\ c_5 B_3(\sigma) + c_6 K_3(\sigma), & \sigma_2 \leqslant \sigma \leqslant a, \end{cases} \tag{45}$$

where $U_0^+ \equiv ig/2(\omega + f)$, $B_j(\sigma)$ and $K_j(\sigma)$ are basic solution functions for layer j, and c_1 to c_6 are constants. If $l_j = 0$ in equation (44b), $B_j(\sigma)$ and $K_j(\sigma)$ are exponentials:

$$\left.\begin{aligned} B_j(\sigma) &= \exp\left[\frac{h(1+i)\sigma}{a-b}\sqrt{\left(\frac{\omega+f}{2E_{z0}\phi(\sigma_{j-1})}\right)}\right] \\ K_j(\sigma) &= \exp\left[\frac{-h(1+i)\sigma}{a-b}\sqrt{\left(\frac{\omega+f}{2E_{z0}\phi(\sigma_{j-1})}\right)}\right] \end{aligned}\right\} \quad \text{for } l_j = 0, \tag{46a}$$

where $\sigma_0 \equiv b$. If $l_j \neq 0$ in equation (44b), $B_j(\sigma)$ and $K_j(\sigma)$ are zeroth-order Kelvin functions:

$$\left.\begin{aligned} B_j(\sigma) &= ber_0\left[\frac{2h}{l_j(a-b)}\sqrt{\left(\frac{\omega+f}{E_{z0}}\phi(\sigma)\right)}\right] + i\, ber_0\left[\frac{2h}{l_j(a-b)}\sqrt{\left(\frac{\omega+f}{E_{z0}}\phi(\sigma)\right)}\right] \\ K_j(\sigma) &= ker_0\left[\frac{2h}{l_j(a-b)}\sqrt{\left(\frac{\omega+f}{E_{z0}}\phi(\sigma)\right)}\right] + i\, ker_0\left[\frac{2h}{l_j(a-b)}\sqrt{\left(\frac{\omega+f}{E_{z0}}\phi(\sigma)\right)}\right] \end{aligned}\right\} \quad \text{for } l_j \neq 0. \tag{46b}$$

The constants c_1 to c_6 are determined from the surface and bottom boundary conditions and by requiring the velocity and stress to be continuous at σ_1 and σ_2. Evaluating these constants gives the velocity solution in final form

$$U^+(\sigma) = \left(1 + \frac{A_1(\sigma)}{A_2'(a)}\right)U_0^+ + \frac{h}{(a-b)E_{z0}\phi(a)}\frac{A_2(\sigma)}{A_2'(a)}\frac{\tau_s^+}{\rho_0}, \tag{47}$$

where

$$A_1(\sigma) = \mu_1(\sigma)\mu_2'(a) - \mu_2(\sigma)\mu_1'(a), \tag{48a}$$

$$A_2(\sigma) = \mu_1(\sigma)\left(\mu_2(b) - \frac{(a-b)E_{z0}\phi(b)}{kh}\mu_2'(b)\right) - \mu_2(\sigma)\left(\mu_1(b) - \frac{(a-b)E_{z0}\phi(b)}{kh}\mu_1'(b)\right), \tag{48b}$$

$$\mu_1(\sigma) = \begin{cases} B_1(\sigma), & b \leqslant \sigma \leqslant \sigma_1, \\ B_1(\sigma_1) + \alpha_1[B_2(\sigma) - B_2(\sigma_1)] + \beta_1[K_2(\sigma) - K_2(\sigma_1)], & \sigma_1 \leqslant \sigma \leqslant \sigma_2 \\ B_1(\sigma_1) + \alpha_1[B_2(\sigma_2) - B_2(\sigma_1)] + \beta_1[K_2(\sigma_2) - K_2(\sigma_1)] & \sigma_2 \leqslant \sigma \leqslant a, \\ \quad + (\alpha_3\alpha_1 + \alpha_4\beta_1)[B_3(\sigma) - B_3(\sigma_2)] + (\beta_3\alpha_1 + \beta_4\beta_1)[K_3(\sigma) - K_3(\sigma_2)], & \end{cases} \tag{49a}$$

$$\mu_2(\sigma) = \begin{cases} K_1(\sigma), & b \leqslant \sigma \leqslant \sigma_1, \\ K_1(\sigma_1) + \alpha_2[B_2(\sigma) - B_2(\sigma_1)] + \beta_2[K_2(\sigma) - K_2(\sigma_1)], & \sigma_1 \leqslant \sigma \leqslant \sigma_2, \\ K_1(\sigma_1) + \alpha_2[B_2(\sigma_2) - B_2(\sigma_1)] + \beta_2[K_2(\sigma_2) - K_2(\sigma_1)] & \sigma_2 \leqslant \sigma \leqslant a, \\ \quad + (\alpha_3\alpha_2 + \alpha_4\beta_2)[B_3(\sigma) - B_3(\sigma_2)] + (\beta_3\alpha_2 + \beta_4\beta_2)[K_3(\sigma) - K_3(\sigma_2)], & \end{cases} \tag{49b}$$

$$\alpha_1 = \frac{B_1(\sigma_1)K_2'(\sigma_1) - B_1'(\sigma_1)K_2(\sigma_1)}{B_2(\sigma_1)K_2'(\sigma_1) - B_2'(\sigma_1)K_2(\sigma_1)}, \tag{50a}$$

$$\alpha_2 = \frac{K_1(\sigma_1)K_2'(\sigma_1) - K_1'(\sigma_1)K_2(\sigma_1)}{B_2(\sigma_1)K_2'(\sigma_1) - B_2'(\sigma_1)K_2(\sigma_1)}, \tag{50b}$$

$$\alpha_3 = \frac{B_2(\sigma_2)K_3'(\sigma_2) - B_2'(\sigma_2)K_3(\sigma_2)}{B_3(\sigma_2)K_3'(\sigma_2) - B_3'(\sigma_2)K_3(\sigma_2)}, \tag{50c}$$

$$\alpha_4 = \frac{K_2(\sigma_2)K_3'(\sigma_2) - K_2'(\sigma_2)K_3(\sigma_2)}{B_3(\sigma_2)K_3'(\sigma_2) - B_3'(\sigma_2)K_3(\sigma_2)}, \tag{50d}$$

$$\beta_1 = \frac{B_2(\sigma_1)B_1'(\sigma_1) - B_2'(\sigma_1)B_1(\sigma_1)}{B_2(\sigma_1)K_2'(\sigma_1) - B_2'(\sigma_1)K_2(\sigma_1)}, \tag{51a}$$

$$\beta_2 = \frac{B_2(\sigma_1)K_1'(\sigma_1) - B_2'(\sigma_1)K_1(\sigma_1)}{B_2(\sigma_1)K_2'(\sigma_1) - B_2'(\sigma_1)K_2(\sigma_1)}, \tag{51b}$$

$$\beta_3 = \frac{B_3(\sigma_2)B_2'(\sigma_2) - B_3'(\sigma_2)B_2(\sigma_2)}{B_3(\sigma_2)K_3'(\sigma_2) - B_3'(\sigma_2)K_3(\sigma_2)}, \tag{51c}$$

$$\beta_4 = \frac{B_3(\sigma_2)K_2'(\sigma_2) - B_3'(\sigma_2)K_2(\sigma_2)}{B_3(\sigma_2)K_3'(\sigma_2) - B_3'(\sigma_2)K_3(\sigma_2)}. \tag{51d}$$

In equations (48)–(51) primes denote derivatives with respect to σ.

Substituting equation (47) into the general relationship between shear stress and velocity (i.e. equation (1) of the text) gives an expression for the shear stress:

$$\frac{\tau^+(\sigma)}{\rho_0} = E_{z0}\phi(\sigma)\left(\frac{a-b}{h}\frac{A_1'(\sigma)}{A_2'(a)}U_0^+ + \frac{1}{E_{z0}\phi(a)}\frac{A_2'(\sigma)}{A_2'(a)}\frac{\tau_s^+}{\rho_0}\right). \tag{52}$$

REFERENCES

1. T. J. Simmons, 'Verification of numerical models of Lake Ontario: Part I. Circulation in spring and early summer', *J. Phys. Oceanogr.*, **4**, 507–523 (1974).
2. Y. P. Sheng, 'Mathematical modeling of three-dimensional coastal currents and sediment dispersion: model development and application', *U. S. Army Corps of Engineers Waterways Experiment Station Rep. CERC-83-2*, 1983.
3. A. F. Blumberg and G. L. Mellor, 'A description of a three-dimensional coastal ocean circulation model', in N. S. Heaps (ed.), *Three-dimensional Coastal Ocean Models*, AGU Press, 1987, pp. 1–16.
4. A. M. Davies, 'Spectral models in continental shelf oceanography', in N. S. Heaps (ed.), *Three-dimensional Coastal Ocean Models*, AGU Press, 1987, pp. 71–106.
5. J. O. Bachus, 'A three-dimensional model for simulation of shelf–sea dynamics', *Dt. Hydrogr. Z.*, **38**, 165–187 (1985).
6. D. E. Dietrich, M. G. Marietta and P. J. Roache, 'An ocean modelling system with turbulent boundary layers and topography: numerical description', *Int. j. numer. methods fluids*, 7, 833–855 (1987).

7. D. B. Haidvogel, J. L. Wilkin and R. Young, 'A semi-spectral primitive equation ocean circulation model using vertical sigma and orthogonal curvilinear horizontal coordinates', *J. Comput. Phys.*, **94**, 151–185 (1991).
8. D. R. Lynch and F. E. Werner, 'Three-dimensional hydrodynamics on finite elements. Part I: Linearized harmonic model', *Int. j. numer. methods fluids*, **7**, 871–909 (1987).
9. D. R. Lynch and F. E. Werner, 'Three-dimensional hydrodynamics on finite elements. Part II: Nonlinear time-stepping model', *Int. j. numer. methods fluids*, **12**, 507–534 (1991).
10. R. A. Walters, 'A three-dimensional finite element model for coastal and estuarine circulation', *Continental Shelf Res.*, **12**, 83–102 (1992).
11. A. M. Davies, 'Application of a three-dimensional turbulence energy model to the determination of tidal currents on the northwest European shelf', *J. Geophys. Res.*, **95**, 18,143–18,162 (1990).
12. N. S. Heaps, 'On the numerical solution of the three-dimensional hydrodynamical equations for tides and storm surges', *Mem. Soc. R. Sci. Liege, Ser. 6*, **2**, 143–180 (1972).
13. R. Lardner, 'Numerical solution of the linearized three-dimensional tidal equations using eddy viscosity eigenfunctions', *J. Geophys. Res.*, **95**, 22,269–22,274 (1990).
14. J. Sheng and K. R. Thompson, 'A modified Galerkin–spectral model for three-dimensional , barotropic, wind-driven shelf circulation', *J. Geophys. Res.*, **98**, 7011–7022 (1993).
15. R. A. Luettich Jr. and J. J. Westerink, 'A solution for the vertical variation of stress, rather than velocity, in a 3-dimensional circulation model', *Int. j. numer. methods fluids*, **12**, 911–928 (1991).
16. K. W. Bowden and S. R. Ferguson, 'Variations with height of the turbulence in a tidally induced bottom boundary layer', in J. C. J. Nihoul (ed.), *Elsiever Oceanography Series*, Vol. 28, *Marine Turbulence, Proc. 11th Liege Colloq. on Ocean Hydrodynamics*, Elsiever, Amsterdam, 1980, pp. 259–286.
17. A. M. Davies, 'On extracting tidal current profiles from vertically integrated two-dimensional hydrodynamic models', *J. Geophys. Res.*, **95**, 18,317–18,342 (1990).
18. H. L. Jenter and O. S. Madsen, 'Bottom stress in wind-driven depth-averaged coastal flows', *J. Phys. Oceanogr.*, **19**, 962–974 (1989).
19. P. D. Craig, J. R. Hunter and B. L. Johnston, 'The implications of a linearly varying eddy viscosity for wind-driven current profiles', *Continental Shelf Res.*, **13**, 1–24 (1993).
20. G. F. Pinder and W. G. Gray, *Finite Element Simulation in Surface and Subsurface Hydrology*, Academic, New York, 1977, p. 67.
21. T. F. Jordan and J. R. Baker, 'Vertical structure of time-dependent flow dominated by friction in a well-mixed fluid', *J. Phys. Oceanogr.*, **10**, 1091–1103 (1980).
22. J. R. Baker and T. F. Jordan, 'Vertical-structure functions for time-dependent flow in a well-mixed fluid with turbulent boundary layers at the bottom and top', *J. Phys. Oceanogr.*, **10**, 1691–1694 (1980).
23. D. R. Lynch and C. B. Officer, 'Analytic test cases for three-dimensional hydrodynamic models', *Int. j. numer. methods fluids*, **5**, 529–543 (1985).
24. A. M. Davies, 'On the accuracy of finite difference and modal methods for computing tidal and wind wave current profiles', *Int. j. numer. methods fluids*, **12**, 101–124 (1991).